

Milanković Forcing in Deep Time

Richard E. Zeebe^{1,*} and Margriet L. Lantink²

*Corresponding Author.

¹School of Ocean and Earth Science and Technology, University of Hawaii at Manoa, 1000 Pope Road, MSB 629, Honolulu, HI 96822, USA. zeebe@soest.hawaii.edu

²University of Wisconsin - Madison, Department of Geoscience, 1215 W. Dayton St., Madison, WI 53706, USA. lantink@wisc.edu

May 3, 2024

Final revised version. In press, *Paleoceanography and Paleoclimatology*

Key Points

- We provide orbital eccentricity, inclination, obliquity, and climatic precession for use in paleostudies/climate models over the past 3.5 Gyr
- The long eccentricity cycle (previously used as "metronome") can become unstable on long time scales
- Earth's past obliquity forcing/amplitude was significantly reduced. We predict reduced obliquity power with age in stratigraphic records

Keywords

Milanković Theory (4969), Astronomical Forcing (4910), Paleoclimatology and Paleooceanography (0473), Sedimentary Geochronology (1165), Astrochronology, Cyclostratigraphy, Solar System

arXiv:2405.00931v1 [astro-ph.EP] 2 May 2024

Abstract

Astronomical (or Milanković) forcing of the Earth system is key to understanding rhythmic climate change on time scales $\gtrsim 10^4$ y. Paleoceanographic and paleoclimatological applications concerned with past astronomical forcing rely on astronomical calculations (solutions), which represent the backbone of cyclostratigraphy and astrochronology. Here we present state-of-the-art astronomical solutions over the past 3.5 Gyr. Our goal is to provide tuning targets and templates for interpreting deep-time cyclostratigraphic records and designing external forcing functions in climate models. Our approach yields internally consistent orbital and precession-tilt solutions, including fundamental solar system frequencies, orbital eccentricity and inclination, lunar distance, luni-solar precession rate, Earth's obliquity, and climatic precession. Contrary to expectations, we find that the long eccentricity cycle (previously assumed stable and labeled "metronome", recent period ~ 405 kyr), can become unstable on long time scales. Our results reveal episodes during which the long eccentricity cycle is very weak or absent and Earth's orbital eccentricity and climate-forcing spectrum are unrecognizable compared to the recent past. For the ratio of eccentricity-to-inclination amplitude modulation (frequently observable in paleorecords) we find a wide distribution around the recent 2:1 ratio, i.e., the system is not restricted to a 2:1 or 1:1 resonance state. Our computations show that Earth's obliquity was lower and its amplitude (variation around the mean) significantly reduced in the past. We therefore predict weaker climate forcing at obliquity frequencies in deep time and a trend toward reduced obliquity power with age in stratigraphic records. For deep-time stratigraphic and modeling applications, the orbital parameters of our 3.5-Gyr integrations are made available at 400-year resolution.

1 Introduction

In 1941, Milanković commented on the motivation for his work on insolation: “If it were actually possible [...] to create a mathematical theory by means of which one could track the effect of insolation in space and time, one would be able to determine the most important basic features of the Earth’s climate computationally.” (Milanković, 1941, see Appendix A). Today, the so-called Milanković cycles are known as periodic changes in Earth’s orbital parameters, causing rhythmic climate change on Earth on time scales $\gtrsim 10^4$ y. Milanković’s primary aim was to apply his astronomical theory to the ice age problem. Since then, numerous studies have investigated the astronomical forcing of climate on time scales ranging from half-precession periods to Gyrs, primarily relying on astronomical calculations/solutions, which today represent the backbone of astrochronology and cyclostratigraphy (for recent summaries, see Montenari, 2018; Himmov, 2018; De Vleeschouwer et al., 2024). While undoubtedly a visionary, Milanković may not have foreseen using digital computer clusters to numerically determine astronomical forcing of Earth’s climate over billions of years of its history (the undertaking of the present study).

Cyclostratigraphy, the study of astronomically induced cycle patterns expressed in stratigraphic sequences, enables reconstructing the Earth System’s intricate response to Milanković forcing and provides a tool for establishing high-resolution temporal frameworks for ordering/dating geologic history (astrochronologies). Beyond ~ 50 Ma, astrochronology may be used to reconstruct the chaotic evolution of orbital cycles such as the unstable, very long eccentricity cycle (~ 2.4 Myr at present, e.g., Olsen et al., 2019; Ma et al., 2017; Zeebe & Lourens, 2019) and in some cases individual fundamental solar system frequencies (e.g. Meyers & Malinverno, 2018; Olsen et al., 2019). Moreover, the cyclostratigraphic record of changing precession and obliquity frequencies permits reconstructing the long-term (tidal) evolution of the Earth-Moon system. The latter approach is especially valuable in Precambrian records, when changes in precession periods and their ratios to eccentricity periods are more pronounced (e.g., Zhang et al., 2015; Meyers & Malinverno, 2018; Lantink et al., 2019, 2022, 2024). However, cyclostratigraphic reconstructions and astrochronology purely based on observational data in deep time is challenging in the absence of astronomical tuning targets due to the uncertain long-term tidal evolution of the Earth-Moon system and the solar system’s chaotic nature (Berger et al., 1989; Laskar et al., 2004; Zeebe, 2017). Conversely, observational studies generate fundamental knowledge and several hard data constraints on the Earth-Moon and solar system history, which in turn, help to constrain the astronomical solutions (e.g. Zeebe & Lourens, 2019; Lantink et al., 2022). Thus, cyclostratigraphic data and astronomical solutions are inherently valuable and in high demand, particularly in deep time.

In this study, we present astronomical solutions from state-of-the-art solar system integrations over the past 3.5 Gyr within a single, internally consistent framework. We highlight important features of the overall nature of, and the dominant frequency components involved in, deep-time Milanković forcing and discuss which cycles may be (un)suitable for developing deep-time astrochronologies. Our astronomical solutions provide examples of possible characteristic forcing patterns to assist in the interpretation of deep-time cyclostratigraphic records and the design of ex-

ternal forcing functions in climate models. We supply two types of internally consistent astronomical solutions, orbital solutions (OSs) and precession-tilt (PT) solutions (see Sections 2 and 3). OS dynamics have important effects on (and are a prerequisite for) PT solutions (the opposite effect is minor, see Section 3.7). For example, amplitude variations in Earth’s orbital inclination (due to OS dynamics) are reflected in obliquity — most evidently during intervals of reduced amplitude variation (see Zeebe, 2022). Similarly, amplitude variations in eccentricity (due to OS dynamics) are reflected in climatic precession. Our combined OS and PT solutions and their analyses yield diagnostic features of deep-time orbital forcing parameters that are also key in more recent cyclostratigraphic and astrochronologic practices. The diagnostics include the different eccentricity cycles (ECs) and the relative periodicities and amplitudes of P: T: SEC: LEC: VLEC (Precession: Tilt: Short EC: Long EC: Very Long EC), as well as the stability of the LEC (previously assumed stable and used as a “metronome” in astrochronology).

1.1 Specific goals, benefits, and outcome provided

Our main goal is to investigate deep-time Milanković forcing and make our results available to the community. Our findings are based on long-term ensemble integrations ($N = 64$, see below), exploring the possible solution/phase space of the solar system. Hence our study provides characteristic features of long-term Milanković forcing and 64 individual solutions, not a single forcing function (as prohibited by dynamical chaos). From our OS and PT solutions, we supply outcome including the fundamental (secular) solar system frequencies (g_i and s_i), lunar distance (a_L), luni-solar precession rate (Ψ), obliquity (ϵ), and climatic precession (\bar{p}) (see Table 1). Importantly, we integrate the equations of motion for Earth’s spin axis over 3.5 Gyr, yielding full solutions for ϵ and \bar{p} (see Section 3). We also include error estimates and a comparison to Waltham (2015)’s results for a_L , Ψ , and averaged ϵ (see Figs. 5 and F2). The results of our 3.5-Gyr OS and PT integrations ($N = 64$), including eccentricity, inclination, obliquity, and climatic precession are made available at 400-year resolution at www.ncei.noaa.gov/access/paleo-search/study/39199 and www2.hawaii.edu/~zeebe/Astro.html.

The present astronomical solutions are designed for deep-time applications (order $t \lesssim -10^8$ y). For the past 100 Myr (300 Myr), we recommend the orbital solutions ZB18a and ZB20x, which have been constrained by geological data and are more accurate on that time scale (Zeebe & Lourens, 2019, 2022b). ZB18a and ZB20x are not incompatible with the current results but feature slightly different attributes, including asteroids and a different timestep. Precession-tilt solutions for the past 100 Myr are available at www2.hawaii.edu/~zeebe/Astro.html and www.ncdc.noaa.gov/paleo/study/35174 and can be generated/customized using `snvec` (github.com/rezeebe/snvec) (Zeebe & Lourens, 2022a).

2 Orbital Solutions

For the orbital solutions, we performed state-of-the-art solar system integrations, including the eight planets and Pluto, a lunar contribution, general relativity, the solar quadrupole moment, and solar mass loss (Zeebe, 2017; Zeebe & Lourens, 2019; Zeebe, 2022; Zeebe, 2023a; Zeebe & Lantink, 2024a). Initial conditions at time t_0 were taken

Table 1. Notation and values used in this paper.

Symbol	Meaning	Value I/A	Unit	Note
ϵ	Obliquity angle			
ϵ_0	Obliquity Earth t_0	23.4392911	deg	Fränz & Harper (2002)
ϕ	Precession angle			
α	Precession constant			see Appendix B
s	Spin vector			unit vector
n	Orbit normal Earth			unit vector
b	Orbit normal Lunar			unit vector
i_L	Inclination lunar orbit			$\cos i_L = (b \cdot n) = y$
ϵ^*	Mutual obliquity			$\cos \epsilon^* = (s \cdot b) = z$
e	Orbital eccentricity			
ϖ	Orbit LP ^a			
$\bar{\omega}$	Orbit LPX ^b			
I	Orbital inclination			
Ω	Orbit LAN ^c			
\bar{p}	Climatic precession			$\bar{p} = e \sin \bar{\omega}$
γ_{gp}	Geodetic precession	-0.0192	"/y	Capitaine et al. (2003)
g_i, s_i	Secular frequencies		"/y	
au	Astronomical unit	$1.495978707 \times 10^{11}$	m	
GM	Sun GP ^d	$1.32712440041 \times 10^{20}$	$\text{m}^3 \text{s}^{-2}$	
$M/(m_E + m_L)$	Mass ratio ^e	328900.5596	-	
m_E/m_L	Mass ratio ^e	81.300568	-	
μ	Lunar GP ^d			$\mu = GM(m_E + m_L)/M$
L	Angular Momentum			
T	Torque			
ω	Earth's angular speed	7.292115×10^{-5}	s^{-1}	at t_0
a_L	Earth-Moon DP ^f		m	
a_{L0}	Earth-Moon DP ^f t_0	3.8440×10^8	m	Quinn et al. (1991)
n_L	Lunar mean motion			$n_L = (\mu/a_L^3)^{1/2}$
A, C	Moments of inertia ^g			
$E_{d0} = (C - A)/C$	Earth's dyn. ellipticity	0.00327381	-	at t_0 , see text
g_L	Lunar orbit factor	0.9925194	-	see text
$\Psi_0 = \phi_0$	Luni-solar prec. t_0	50.384815	"/y	Capitaine et al. (2003)
m_E	Mass Earth	5.9720×10^{24}	kg	
R_E	Radius Earth	6378.136×10^3	m	
k_s	Love No. Secular	0.942	-	^h
k_2	Love No. TE ^k	0.3	-	^h
Δt_t	Tidal time lag			Mignard (1981)
δ	Tidal phase lag			^h
K	Solar factor for α ^l			see Appendix B
β	Lunar factor for α ^l			see Appendix B

^a LP = Longitude of Perihelion. ^b LPX = LP from the moving equinox. ^c LAN = Longitude of Ascending Node. ^d GP = Gravitational Parameter. ^e Index E = Earth, L = Lunar. ^f DP = Distance Parameter. ^g Earth's equatorial (A) and polar (C) moment of inertia. ^h For details, see MacDonald (1964); Goldreich (1966); Lambeck (1980); Baenas et al. (2019). ^k TE = tidal-effective. ^l Factors for α related to solar and lunar torque (see Appendix B).

from the latest JPL ephemeris DE441 (Park et al., 2021) and the equations of motion were numerically integrated to $t = -3.5$ Gyr (beyond -3.5 Gyr very few geologic records are available and parameters such as the lunar distance have large uncertainties, see Section 3.7). Owing to solar system chaos, the solutions diverge around $t = -50$ Myr, which prevents identifying a unique solution on time scales $\gtrsim 10^8$ y, see (Laskar et al., 2004; Zeebe, 2017; Zeebe & Lourens, 2019, 2022b). Hence we present results from long-term ensemble integrations to explore the possible solution/phase space of the system. Importantly, because of the chaos, each $\sim 10^8$ y interval of the integrations represents a snapshot of the system’s general/possible behavior that is largely independent of the actual numerical time of a particular solution (provided here that $t < -\tau_{12}$, where τ_{12} is of order 10^8 to 10^9 y, see below). In other words, a numerical solution’s behavior around, say, $t = -1.5$ Gyr may represent the actual solar system around $t = -600$ Myr and so on. Our approach allows for full solar system dynamics and full dynamical chaos and is fundamentally different from Hoang et al. (2021) who used a simplified, secular model (truncated at 2nd order in masses and 5th order in eccentricities/inclinations).

2.1 Numerical integrator and physical setup

Solar system integrations were carried out following our earlier work (Zeebe, 2015a; Zeebe, 2015b; Zeebe, 2017; Zeebe & Lourens, 2019; Zeebe, 2022) with our integrator package orbitN (v1.0) (Zeebe, 2023a). The open source code is available at doi.org/10.5281/zenodo.8021040 and github.com/rezebe/orbitN. The methods, physical setup, and our integrator package used here have been extensively tested and compared against other studies (Zeebe, 2017; Zeebe & Lourens, 2019; Zeebe, 2022; Zeebe, 2023a); for more information, see Appendix C.

2.2 Ensemble integrations

We performed ensemble integrations of the solar system with a total of $N = 64$ members. Note that a larger N is not necessarily advantageous for the current application. For one, our goal is to explore the system’s general behavior and provide an abundance of possible values for the fundamental solar system frequencies (secular g - and s -frequencies). For instance, time series analysis of consecutive 20-Myr intervals of our simulations (see below) provide $64 \cdot (3,500/20) = 11,200$ values for each frequency, which is plenty. The analysis of some frequencies is cumbersome and requires individual inspection and manual work (see below), which becomes unfeasible for large N . Also, regarding the occurrence of, e.g., σ_{12} resonances (see Appendix D and Zeebe & Lantink (2024a)), our ensemble integrations sample a frequently occurring phenomenon ($\sim 40\%$ of solutions), not a rare event such as the destabilization of Mercury’s orbit, which would require large N (e.g., Laskar & Gastineau, 2009; Zeebe, 2015b; Abbot et al., 2023). The fact that the σ_{12} resonance was (1) recognized previously (Lithwick & Wu, 2011; Mogavero & Laskar, 2022) — although not its effect on the LEC (see Zeebe & Lantink, 2024a) — and (2) found in $\sim 40\%$ of our solutions suggests that entering the σ_{12} resonance on long time scales is a common (not rare) dynamical feature. Different solutions were obtained by offsetting Earth’s initial position by a small distance (largest offset $\Delta x_0 \simeq 1 \times 10^{-12}$ au), which is within observational uncertainties (Zeebe, 2015b; Zeebe, 2017). The differ-

ent Δx_0 lead to complete randomization of solutions on a time scale of ~ 50 Myr due to solar system chaos. We also tested different histories of the Earth-Moon distance (a_L), which has little effect on our OS results (see Section 3.7). Because of scarce geological records and the large uncertainties in a_L prior to ~ 3.5 Ga, we restrict our integrations to $t = -3.5$ Gyr. Our solutions are available at www.ncei.noaa.gov/access/paleo-search/study/39199 and www2.hawaii.edu/~zeebe/Astro.html.

2.3 Past Earth-Moon distance

Our solar system integrations include a lunar contribution, i.e., a gravitational quadrupole model of the Earth-Moon system (Quinn et al., 1991; Varadi et al., 2003; Zeebe, 2017; Zeebe, 2023a). The lunar contribution has a relatively small effect on the overall orbital dynamics of the solar system, yet the integration requires the Earth-Moon distance (a_L) as a parameter at a given time in the past (details and technical aspects are discussed in Section 3.7).

2.4 Time series analysis of astronomical solutions

The solar system’s fundamental g - and s -frequencies (aka secular frequencies) were determined from the output of our numerical integrations using fast Fourier transform (FFT) over consecutive 20-Myr intervals. For the spectral analysis, we used Earth’s orbital elements and the classic variables:

$$\begin{aligned} h &= e \sin(\varpi) & ; & & k &= e \cos(\varpi) & (1) \\ p &= \sin(I/2) \sin \Omega & ; & & q &= \sin(I/2) \cos \Omega, & (2) \end{aligned}$$

where e , I , ϖ , and Ω are eccentricity, inclination, longitude of perihelion, and longitude of ascending node, respectively. The variables h , k , p , q are useful analytically and obey the relationships $h^2 + k^2 = e^2$ and $p^2 + q^2 = \sin^2(I/2)$ (e.g., Murray & Dermott, 1999). The spectra for Earth’s h , k and p , q , for example, show strong peaks at nearly all g - and s -frequencies, respectively (see Zeebe & Lantink, 2024a), i.e., analyzing only Earth’s spectrum may suffice (instead of all planetary spectra), depending on the application. The g - and s -modes are loosely related to the apsidal and nodal precession of the planetary orbits (see Zeebe & Lantink, 2024a). However, there is generally no simple one-to-one relationship between a single mode and a single planet, particularly for the inner planets. The system’s motion is a superposition of all modes, although for the outer planets, some modes are dominated by a single planet.

3 Precession-Tilt Solutions and Framework

3.1 Theoretical PT framework and previous studies

The current approach provides combined OS and PT solutions, the latter of which are obtained within a theoretical framework (Framework I hereafter) that has been applied to the Earth-Moon system, Pluto-Charon, exoplanets, etc. (e.g., MacDonald, 1964; Goldreich, 1966; Mignard, 1981; Touma & Wisdom, 1994; Atobe & Ida, 2007; Cheng et al., 2014; Downey et al., 2023). The emphasis is on long-term physical solutions for the planetary spin axis, the satellite’s orbital inclination, and (here) explicit obliquity and precession solutions. In a number of related, but somewhat distinct studies, the emphasis has

shifted toward a detailed model framework for the Earth-Moon’s tidal evolution (Framework II hereafter), particularly the history of ocean tidal dissipation (e.g., Webb, 1982; Hansen, 1982; Kagan & Maslova, 1994; Motoyama et al., 2020; Daher et al., 2021; Tyler, 2021; Farhat et al., 2022). The advance in modeling past ocean tidal evolution provided by these studies is clearly desirable. Importantly, however, studies of both frameworks (regardless of emphasis) ultimately rely on fitting results to external parameters and observational data in order to provide realistic astronomical parameters such as lunar distance, precession frequency, etc. on Gyr-time scale. For instance, Daher et al. (2021) explore tidal energy dissipation rates based on reconstructed basin paleogeometries but are unable to collapse the lunar distance to near zero at ~ 4.4 Ga (lunar age). Tyler (2021) fits two parameters (effective ocean depth and dissipation time scale) to observational data including length of day/month and lunar distance. Farhat et al. (2022) also fit two parameters (uniform effective ocean depth and effective dissipation frequency) to the lunar age and the present lunar recession rate. In addition, Farhat et al. (2022) assume a smooth transition from a global ocean planet prior to 1 Ga. Unfortunately, observational data to verify or falsify the different tidal evolution models are extremely sparse, especially prior to ~ 1 Ga. If restricted to robust data sets from cyclostratigraphic studies, only two data points are available with ages older than 1 Ga (see Fig. 1b). For more information on the cyclostratigraphic studies (Meyers & Malinverno, 2018; Lantink et al., 2022; Sørensen et al., 2020; De Vleeschouwer et al., 2023), see Section 3.7.

As detailed below, the current approach to obtain PT solutions follows Framework I, using an internally consistent physical model with a single fit parameter, the tidal time lag Δt_t (Mignard, 1981; Touma & Wisdom, 1994). Analog to Framework II, Δt_t is fit to match theoretical results with observational data (here cyclostratigraphic data for the lunar distance, see Fig. 1). At this time, no observational evidence is available to decide whether Framework I or II provides more accurate/realistic results for the current application over the full past 3.5 Gyr. For the present theoretical approach (PT solutions), Framework I is much preferred because the necessary assumptions and mathematical approach can be stated clearly and succinctly (see Section 3 and Appendix E). If desired, results of tidal evolution models may be evaluated within the current framework (see Appendix F, Fig. F1).

3.2 Precession-Tilt Solutions

The precession-tilt (PT) solutions computed here are based on our earlier work (Zeebe & Lourens, 2022a; Zeebe, 2022) using the `snvec` code, see github.com/rezebee/snvec and Appendix B. The original `snvec` code was developed to provide PT solutions over the past 100 Myr or so, following Quinn et al. (1991). While the code includes parameters for tidal dissipation and dynamical ellipticity, it lacks proper dynamical equations for the long-term evolution of the Earth-Moon system (including non-linear evolution of lunar distance, Earth’s spin, luni-solar precession, etc.). Hence we added several features and differential equations to provide PT solutions on Gyr-time scale. The integration of the long-term precession equations follows the classical work of MacDonald (1964); Goldreich (1966); Mignard (1981), shown to capture the essential dynamics (e.g., Touma & Wisdom, 1994) and ap-

propriate for a variety of applications (e.g., Atobe & Ida, 2007; Cheng et al., 2014; Downey et al., 2023), as well as the current one (see below).

3.3 Differential equations for L and a_L

We added differential equations to the `snvec` code for the magnitude of Earth’s angular momentum L and the Earth-Moon (lunar) distance a_L . For variables and symbols, see Table 1. The equation for L reads (see Section 3.5 and Goldreich, 1966):

$$\dot{L} = T_E \cdot s = T_2 \sin \epsilon^* + T_3 \cos \epsilon^*, \quad (3)$$

where the mutual obliquity ϵ^* is the angle between Earth’s spin (unit) vector s and the lunar orbit normal b ; T_2 and T_3 are torque components (see Section 3.5 and Appendix E). The current application does not require resolving the lunar orbit precession (~ 18.6 y). Hence for the time-averaged lunar orbit normal, we may take $\bar{b} \simeq \bar{n}$, where n is Earth’s orbit normal (in that approximation, $\bar{\epsilon}^* \simeq \epsilon$). The equation for a_L reads (Goldreich, 1966):

$$\dot{a}_L = 2 a_L T_L \cdot b / l = 2 a_L T_{3L} / (m_L \sqrt{\mu a_L}), \quad (4)$$

where $T_{3L} = -T_3$ (see Section 3.5 and Appendix E), $l = m_L \sqrt{\mu a_L}$ is the lunar angular momentum and $\mu = GM \cdot (m_E + m_L) / M$. Integration of the above differential equations yield $a_L(t)$ and $\omega(t) = L(t) / C(t)$, from which K , β , α , and Ψ can be calculated (see Eq. (15) and Appendix B). For error estimates and a comparison to Waltham (2015)’s results for a_L , Ψ , and averaged ϵ , see Figs. 5 and F2.

3.4 Moment of Inertia

Earth’s angular spin, ω , is calculated from $L = C\omega$, where C is the moment of inertia (MacDonald, 1964; Goldreich, 1966):

$$C = I \{1 + (2k_s R_E^5 / 9GI) \omega^2\} \quad (5)$$

and $I = 0.33 m_E R_E^2$. Note that C depends on ω , yet changes in ω and C are small per integration step. Thus, numerically it suffices to update $\omega = L/C$ and Eq. (5) each time the derivative routine is called, which occurs multiple times per integration step.

3.5 Tidal friction equations

The tidal friction equations in, e.g., Goldreich (1966) and Touma & Wisdom (1994) are given in terms of obliquity/inclination angles. However, our `snvec` code integrates differential equations for Earth’s spin vector s (see Quinn et al., 1991; Zeebe & Lourens, 2022a; Zeebe, 2022). In the following, we therefore derive a tidal friction equation for s . Let’s write Earth’s angular momentum vector as:

$$L = Ls, \quad (6)$$

where (as mentioned above) s is a unit vector. It follows for the torque ($dL/dt = T_E$):

$$d/dt(Ls) = \dot{L}s + L\dot{s} = T_E. \quad (7)$$

Now dot Eq. (7) by s and note that $s \cdot s = 1$. Also, for s to remain a unit vector, any change must be perpendicular, i.e., $\dot{s} \cdot s = 0$ and hence:

$$\dot{L} = T_E \cdot s. \quad (8)$$

Inserting into Eq. (7) then yields an equation for \dot{s} , as desired:

$$\dot{s} = [T_E - (T_E \cdot s) s] / L. \quad (9)$$

The T_E terms are given by ($T_1 = 0$, see Appendix E for T_2 and T_3):

$$T_E = T_1 e_1 + T_2 e_2 + T_3 e_3 \quad (10)$$

$$T_E \cdot s = T_2 \sin \epsilon^* + T_3 \cos \epsilon^*, \quad (11)$$

where the e_i are unit vectors forming a coordinate system in which the torque components are conveniently expressed (Goldreich, 1966). The e_i are given by (e'_i are used to project T'_i , see Appendix E):

$$e_1 = (s \times b) / \sin \epsilon^*; \quad e_2 = (s - b \cos \epsilon^*) / \sin \epsilon^*; \quad (12)$$

$$e'_1 = (s \times n) / \sin \epsilon; \quad e'_2 = (s - n \cos \epsilon) / \sin \epsilon; \quad (13)$$

$$e'_3 = n.$$

3.6 Tidal torques

Within the present framework, it is possible to use different tidal torque expressions (e.g., MacDonald, 1964; Goldreich, 1966; Mignard, 1981; Touma & Wisdom, 1994). For the most part, the differences obtained for the different torque expressions are relatively small for $a_L \gtrsim 30R_E$, except for Earth's obliquity. Over this range (which is explored here), uncertainties in the tidal friction evolution (if unconstrained by data) are usually larger than those arising from the torque expressions. We have tested two sets of torques (Mignard's and MacDonald's torques, see Appendix E for equations) and implemented both in the snvec code. MacDonald's torques are relatively easy to implement but do not include solar tides and solar-lunar cross terms (see Touma & Wisdom, 1994). Also, some fundamental issues with MacDonald's approach have been noted (e.g. Efroimsky & Makarov, 2013). More importantly, the solar-lunar cross terms (not included in MacDonald's torques) have a significant effect on the obliquity evolution and tend to align the spin axis with the orbit normal, which is relevant here (see Fig. 5). Hence we selected Mignard's tidal torques, including cross terms, as our default option (see Mignard, 1981; Touma & Wisdom, 1994, and Appendix E).

3.7 Tidal friction in the past

Before discussing tidal friction in the past, we first explain a technical aspect of our approach. The PT solution provides the lunar distance, a_L , at a given time in the past (see Eq. (4)), based on which precession and obliquity are computed. Now solving the PT equations requires output from the OS as input, while the OS requires a_L as input for the gravitational quadrupole model of the Earth-Moon system (Quinn et al., 1991; Varadi et al., 2009; Zeebe, 2017; Zeebe, 2023a). Importantly, however, the lunar contribution has a relatively small effect on the overall OS dynamics. Furthermore, in terms of computations and data handling, it is much more convenient to run OS and PT integrations separately. Thus, we prescribed a_L as input for the OS (including different options, see below) and performed ensemble integrations for the orbital part first. Next, we used the OS output as input for the PT integrations, which allowed for easy parameter variations. For the prescribed a_L (OS input), we included an option based

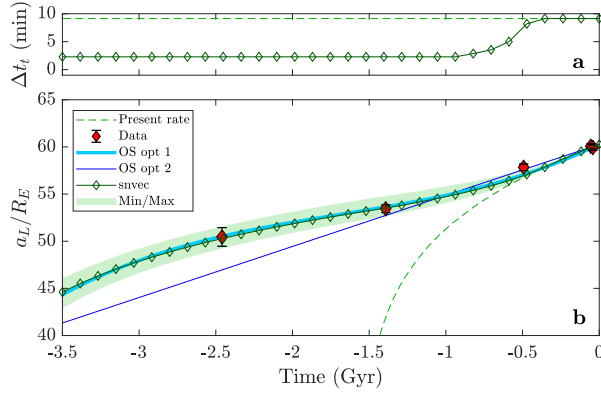


Figure 1. (a) Tidal time lag Δt_i (diamonds) used in Mignard's torques including solar-lunar cross terms (see Appendix E). Dashed line shows constant (present) Δt_i . (b) Past Earth-Moon distance (a_L) in units of Earth radii (R_E). Red diamonds: Observational estimates based on robust data sets from cyclostratigraphic studies (see Section 3.7). Cyan and blue lines: Options 1 and 2 used in the orbital solution (OS). Blue: linear extrapolation into the past starting with \dot{a}_L close to the present rate. Cyan: 3rd-order polynomial fit to observations (see Eq. (14)). Using a_L based on the blue and cyan lines made essentially no difference in our OSs (see text Section 3.7). Green lines/symbols: Integration of precession equations with snvec. Light green area (Min/Max): Error envelope for a_L reflecting cyclostratigraphic data errors, see Section 3 and Fig. F2. Green dashed: starting at present rate $\dot{a}_{L0} = 3.82 \text{ cm y}^{-1}$ with constant tidal time lag ($\Delta t_i \approx 9 \text{ min}$) in the past (see (a)), yields the (well-known) unrealistic past a_L . Dark green diamonds: using variable Δt_i in the past from (a), internally consistent with OS option 1, see text.

on observational data (see Fig. 1) that is internally consistent between OS and PT solution.

Integration of the classic precession equations with snvec (see Sections 3.3-3.6) and a constant (present) tidal time lag of $\Delta t_i \approx 9 \text{ min}$ ($\dot{a}_{L0} = 3.82 \text{ cm y}^{-1}$) leads to the well-known problem of unrealistically small a_L in the past (Fig. 1, green dashed line). Thus, for the PT integrations, we used a variable Δt_i in the past (Fig. 1a) that yields a_L consistent with both observational data and the prescribed a_L input option 1 for the OS (Fig. 1b). (For an alternative Δt_i history and evaluation of tidal evolution models, see Fig. F1.) Note that due to its small effect, selecting OS input option 1 or 2 for a_L made essentially no difference in our long-term OS ensembles. For the observational constraints, we selected robust data sets based on the reconstruction of Earth's axial precession frequency obtained by cyclostratigraphic studies (Meyers & Malinverno, 2018; Lantink et al., 2022; Sørensen et al., 2020; De Vleeschouwer et al., 2023) (Fig. 1b). Other methods for estimating past a_L (and precession frequency) include the analysis of tidal rhythmites and fossil growth laminae, but these approaches are generally associated with large uncertainties and ambiguities in interpretation, especially for Precambrian time intervals (Lantink et al., 2022; Laskar et al., 2024). Our selection of cyclostratigraphic a_L estimates was based on two main quality criteria (for further discussion, see Sinnesael et al., 2019). (1) The presence of clearly developed, visually identifiable rhythms in studied proxy records, exhibiting expected Milanković cycle (period) ratios and amplitude modulation relationships, supported by results of time-series analysis and statistical hypothesis testing (i.e., records with a high signal-to-noise ratio). (2) Consideration of additional chronostratigraphic data (e.g., radioisotopic ages, magnetostratigraphy, biostratigraphy) that independently support Milanković interpretations of observed stratigraphic patterns.

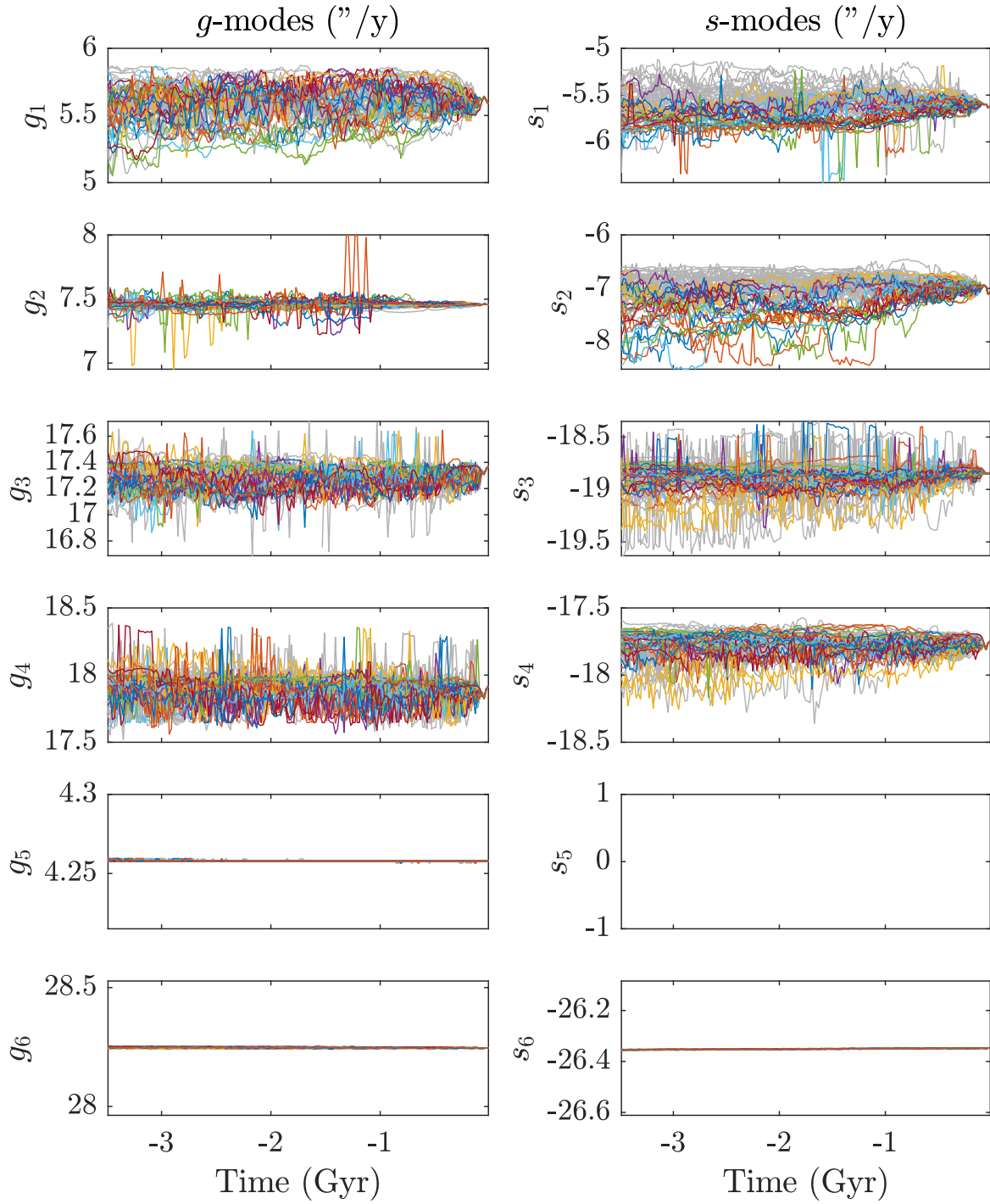


Figure 2. Evolution of fundamental (secular) solar system frequencies. The g - and s -frequencies (in $\text{arcsec y}^{-1} = \text{\"/y}$) were determined from our solar system integrations using fast Fourier transform (FFT) over consecutive 20-Myr intervals and Earth's k and q variables (see text). The g - and s -modes are loosely related to the apsidal and nodal precession of the planetary orbits. Solutions including σ_{12} -resonance intervals ($\sim 40\%$) are highlighted in color (see Appendix D and Zeebe & Lantink, 2024a), the remaining solutions are displayed in gray.

A 3rd order polynomial fit to observations across the interval $t = [-3.5, 0]$ Gyr is:

$$(a_L/a_{L0})^{\text{fit}} = 1 + q_1 t + q_2 t^2 + q_3 t^3, \quad (14)$$

where $\mathbf{q} = [0.1312, 0.05197, 0.01031]$ and t is in Gyr (≤ 0). Importantly, the prescribed fit is only used for the OS, not the PT integration, where a_L is calculated using Δt_t (Fig. 1a).

3.8 Luni-solar precession rate

The luni-solar precession rate Ψ (see e.g., Williams, 1994) may be calculated from (Quinn et al., 1991):

$$\Psi = -\dot{\phi} = -d\phi/dt = K(\kappa + \beta) \cos \epsilon + \gamma_{gp}, \quad (15)$$

where ϕ and ϵ are the precession and obliquity angles ($d\phi/dt = 0$, retrograde precession along the ecliptic), $K(\kappa + \beta) = \alpha$ is the precession constant (see Appendix B), and γ_{gp} is the geodetic precession (see Table 1 and Zeebe (2022)). Note that Eq. (15) strictly only applies at t_0 and does not capture certain periodic variations.

4 Results

4.1 g - and s -frequencies

From our 3.5-Gyr orbital integrations, we determined the solar system's fundamental g - and s -frequencies (f 's, aka modes) using fast Fourier transform (FFT) over consecutive 20-Myr intervals (Fig. 2). The analysis is straightforward for practically stable frequencies such as g_5 , g_6 , and s_6 . However, for full numerical solar system integrations and nearby, changing frequencies such as g_3 and g_4 , and s_3 and s_4 , the analysis is not fail-safe and cumbersome, and requires individual inspection and manual work. For example, one may set up an automated search within a given window for each f . However, as f 's evolve over time, some nearby f 's cross into adjacent search windows (f ranges overlap). In addition, some spectral peaks split into two peaks across certain time intervals and their power varies substantially. Hence the results of an automated search for g_3 , g_4 , s_3 , and s_4 may yield ambiguous or incorrect results that need to be manually corrected by adjusting the center and/or width of the search window. We have checked many but not all of our results for g_3 , g_4 , s_3 , and s_4 displayed in Fig. 2 (total of $64 \cdot (3,500/20) \cdot 4 = 44,800$ values). Thus, while the overall patterns for g_3 , g_4 , s_3 , and s_4 are robust, a few erroneous assignments may be possible. For g_1 , g_2 , s_1 , and s_2 assignment is not an issue because their f ranges generally do not overlap. Values for $s_1 \lesssim -6.2''/y$ (which could interfere with s_2) occurred during so-called σ_{12} -resonance intervals and were confirmed manually. The secular resonance $\sigma_{12} = (g_1 - g_2) + (s_1 - s_2)$ is dominated by Mercury's and Venus' orbits and can cause the long eccentricity cycle (LEC) to become unstable over long time scales (see Appendix D and Zeebe & Lantink (2024a)).

The frequencies g_1 , s_1 , and s_2 drift most strongly over time owing to chaotic diffusion. In addition, g_2 shows large and rapid shifts (spikes) at specific times when the spectral g_2 peak splits into two peaks at significantly reduced power during σ_{12} -resonance episodes. Alternating maximum power between the two peaks then causes the spikes in g_2 . As a result, $g_{25} = (g_2 - g_5)$ is unstable and weak/absent during σ_{12} -resonance intervals. g_5 , g_6 ,

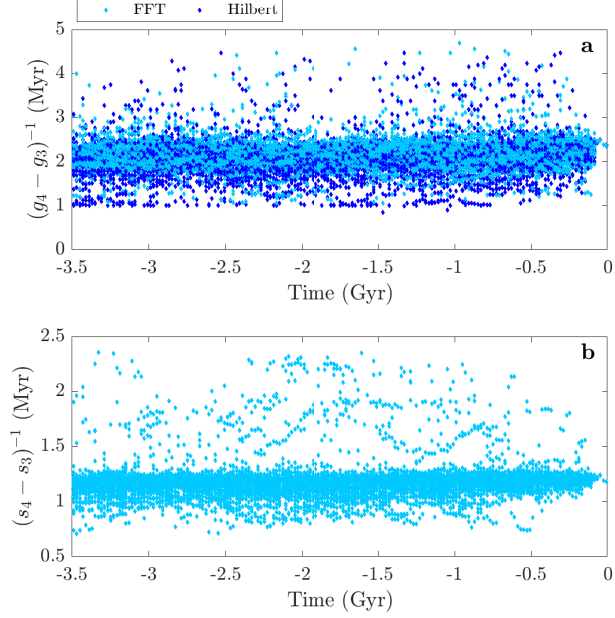


Figure 3. Periods of $(g_4 - g_3)$ and $(s_4 - s_3)$ over consecutive 20-Myr intervals based on our solar system integrations. Light blue: from individual g 's and s 's obtained by direct FFT (see Fig. 2). (a) Dark blue: $(g_4 - g_3)^{-1} = \text{VLEC}$ from spectral analysis of the Hilbert transform of a 100-kyr filter of eccentricity (see Figs. 13 and 14 of Zeebe et al., 2017). For $(s_4 - s_3)$, the Hilbert transform method (using filtered inclination) often fails because it tends to overemphasize long periods in the Hilbert transform. For $(s_4 - s_3)$ it frequently predicts a period doubling (not shown), inconsistent with individual s 's from FFT.

and s_6 (dominated by Jupiter and Saturn) are practically stable over 3.5 Gyr (s_5 is zero due to conservation of total angular momentum/existence of an invariable plane).

4.2 Amplitude modulation: $(g_4 - g_3)$ and $(s_4 - s_3)$

The frequency combinations $(g_4 - g_3) = g_{43}$ and $(s_4 - s_3) = s_{43}$ cause amplitude modulations (AM) in eccentricity and inclination, respectively, at a period of about 2.37 and 1.18 Myr in the recent past. Note that g_{43} 's period is also referred to as VLEC. The frequency ratios are associated with a secular resonance (hereafter σ_{43}) at a recent $g_{43}:s_{43}$ ratio of 1:2, or period ratio of 2:1. We tested two different methods (FFT and Hilbert transform), to determine the periods of g_{43} and s_{43} in our 3.5-Gyr integrations, which yielded somewhat different results for the period distributions (see Figs. 3 and 4), which, again is an expression of the fact that the analysis of g_3 , g_4 , s_3 , and s_4 is not straightforward in all cases (see above). The most frequent g_{43} period in our 3.5-Gyr integrations is ~ 2.1 Myr (Fig. 4a), and not ~ 2.37 Myr as in the recent past. In contrast, the most frequent s_{43} period is in fact ~ 1.2 Myr (Fig. 4c), as in the recent past. As a result, there is a significant peak in the $s_{43}:g_{43}$ ratio distribution at $\sim 1.8:1$ ($2.1/1.2 \approx 1.8$, see Fig. 4d). Nevertheless, in total there are more $s_{43}:g_{43}$ combinations closer to the resonance ratio of 2:1 than at 1.8:1.

Importantly, there is a wide distribution around the 2:1 ratio (see Fig. 4d), i.e., the system is not restricted to an exact 2:1 resonance state. In addition, the σ_{43} secu-

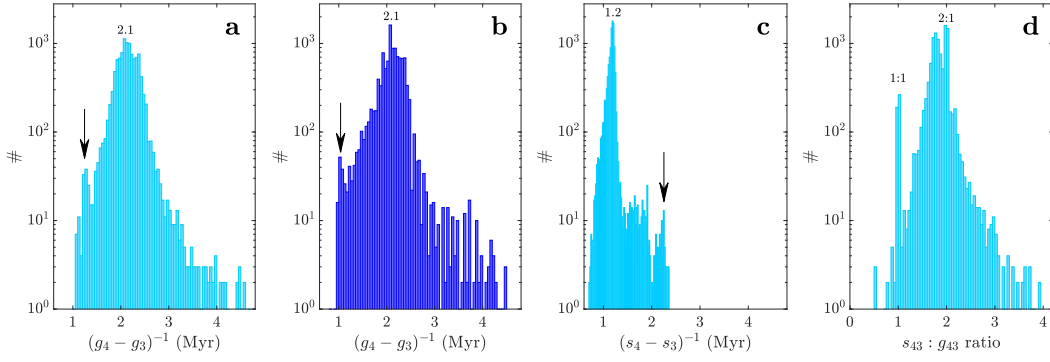


Figure 4. Histograms for the $g_{43} = (g_4 - g_3)$ and $s_{43} = (s_4 - s_3)$ periods (see Fig. 3). Note the logarithmic y-scale. (a) $g_{43}^{-1} = \text{VLEC}$ from direct FFT (max at 2.1 Myr). The side peak at ~ 1.25 Myr (arrow) has been confirmed in various solutions and contributes to the 1:1 $s_{43}:g_{43}$ ratio marked in (d). (b) g_{43}^{-1} based on Hilbert transform (max at 2.1 Myr). Arrow: same as in (a). The peak around 3.8 Myr is not robust because the method tends to overemphasize long periods in the Hilbert transform. (c) s_{43}^{-1} from direct FFT (max at 1.2 Myr). The side peak at ~ 2.25 Myr (arrow) has been found in a few solutions ($g_{43}^{-1} \approx 2.2$ Myr simultaneously) and contributes to the 1:1 $s_{43}:g_{43}$ ratio as well. (d) $s_{43}:g_{43}$ ratio from direct FFT.

lar resonance may switch to a 1:1 ratio, although we found the 1:1 ratio to be ~ 6 times less frequent than the 2:1 ratio for the 20-Myr intervals analyzed (Fig. 4d). Non-integer ratios of $s_{43}:g_{43}$ (say different from 2:1 and 1:1) do not only occur while the system transitions between the resonance (integer) ratios 2:1 and 1:1. For example, in some of our solutions, the system hovers around the 1.8:1 state for tens of millions of years and returns to the 2:1 state without transitioning to the 1:1 state in between. Also, ratios $> 2:1$ are common (Fig. 4d) without transitioning to a potentially higher resonance. VLEC values (g_{43} periods) anywhere between, say 1.2 and 2.8 Myr inferred from deep-time records (e.g., Olsen et al., 2019) and $s_{43}:g_{43}$ ratios between, say 1:1 and 2.5:1 should not come as a surprise (Fig. 4).

4.3 Precession-Obliquity evolution

Given a history of the tidal time lag in the past (see Fig. 1) and the OS output as input to the PT routine, precession and obliquity can be computed over the past 3.5 Gyr for a given OS (Fig. 5). The computed evolution of the lunar distance (a_L , Eq. (4)) and luni-solar precession rate (Ψ , Eq. (15)) are nearly the same for all OS ensemble members. The lunar distance increases by $\sim 35\%$ and the luni-solar precession period more than triples over 3.5 Gyr (Fig. 5a and b). Obliquity (ϵ) and climatic precession ($\bar{p} = e \sin \bar{\omega}$), however, show differences depending on the OS. For example, amplitude variations in Earth’s orbital inclination (due to OS dynamics) are reflected in ϵ — most evidently intervals of reduced amplitude variations (see arrows, Fig. 5c) (cf. Zeebe, 2022). Similarly, amplitude variations in eccentricity (due to OS dynamics) are reflected in \bar{p} . For instance, the eccentricity amplitude may be reduced during σ_{12} -resonance episodes, which is directly passed on to \bar{p} (see Fig. 5d), as eccentricity is the envelope of climatic precession.

The details of the torque physics are relevant for Earth’s obliquity. Mignard’s torques including solar-lunar cross-terms (Mignard, 1981; Touma & Wisdom, 1994) significantly elevate mean ϵ at a given a_L (or time) in the past, relative to MacDonald’s torques (Fig. 5c). The cross-terms tend to align the spin axis with the orbit normal (see Touma & Wisdom, 1994). Note that an overall lower obliquity in the past has been discussed in the literature, although the details differ (e.g., MacDonald, 1964; Goldreich, 1966; Laskar et al., 2004; Daher et al., 2021; Farhat et al., 2022).

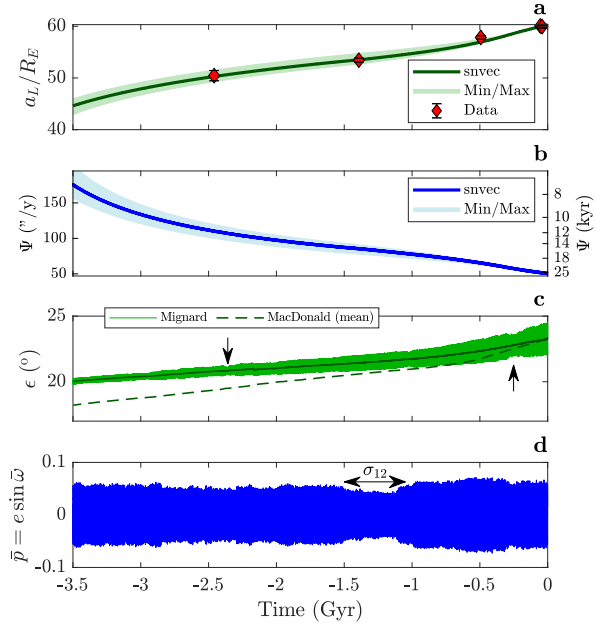


Figure 5. PT solution based on the OS from run R06. Error envelopes in (a) and (b) are based on estimated lunar distance uncertainties (reflecting the cyclostratigraphic data errors, see panel (a) and Fig. F2). (a) Lunar distance (a_L) in units of Earth radii (R_E). Green line: PT solution obtained using *snvec* code. Red diamonds: Observational estimates based on robust data sets from cyclostratigraphic studies (see Section 3.7). (b) Luni-solar precession rate (Ψ , see Eq. (15)) in arcsec y^{-1} (left axis) and period in kyr (right axis). (c) Obliquity ϵ calculated with Mignard’s torques including cross-terms (light green) and MacDonald’s torques (dashed, binned mean values). Arrows highlight selected intervals of reduced amplitude variations in orbital inclination and hence in ϵ . Also note the general trend of increasing ϵ amplitude with time (see text). (d) Climatic precession ($\bar{p} = e \sin \bar{\omega}$). Reduced amplitude variations in orbital eccentricity (and hence in \bar{p}) may occur during σ_{12} -resonance episodes (double arrow, see Appendix D and Zeebe & Lantink (2024a)).

Importantly, and regardless of the torque details, our computations show that Earth’s obliquity (ϵ) was lower and its amplitude (variation around the mean) significantly reduced in the past. The reason for the reduced amplitude is the interplay between the luni-solar precession (Ψ) and the periodic motion of Earth’s orbit plane with reference to inclination. Consider the variations in inclination (secular frequencies s_i) as a forcing acting on the precession motion of the spin axis (s). If $\Psi \gg s_i$, s closely follows the orbit plane (while precessing), ϵ is constant and

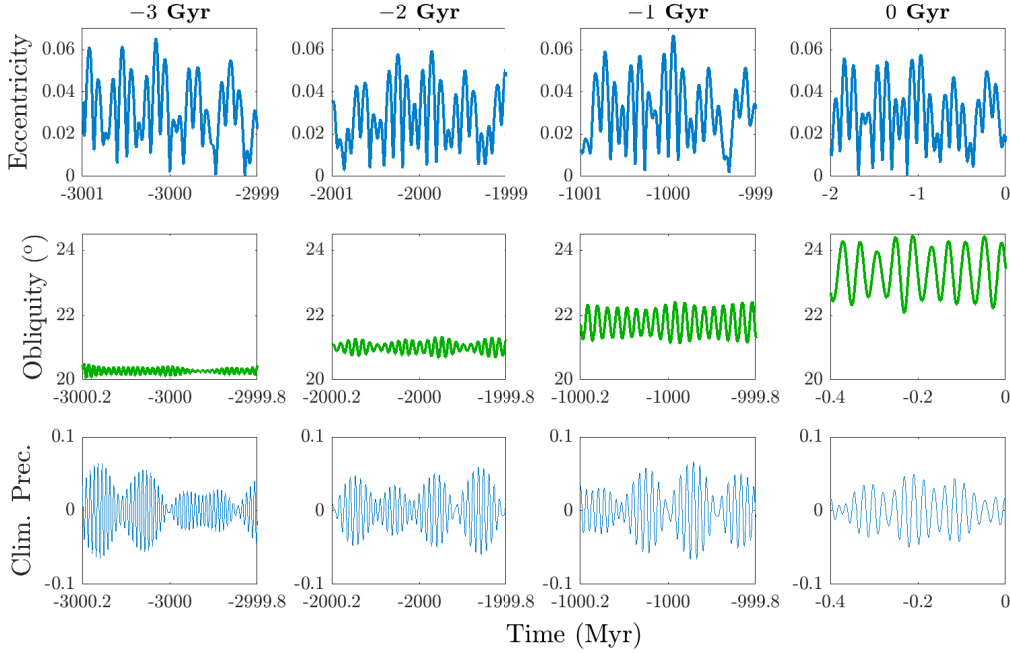


Figure 6. Example of ETP behavior from solution R02. Top row: Eccentricity over 2-Myr intervals centered around -3 , -2 , -1 , and 0 Gyr. Middle row: Obliquity over 400-kyr intervals. Bottom row: Climatic precession ($\dot{\beta} = e \sin \omega$) over 400-kyr intervals. Note that $\dot{\beta}$'s amplitude around 0 Gyr (bottom-right) is smaller than at older time intervals because it happens to coincide with a smaller 405-kyr eccentricity maximum in the most recent past (see eccentricity, top-right).

the amplitude (variation) \sim null (past limit). If $\Psi \approx s_i$, the two motions become resonant and ϵ 's amplitude is large (future). To first order, the amplitude (say B) is proportional to $s_i/(s_i + \Psi)$ (Ward, 1974, 1982). Thus, the amplitude ratio at two different Ψ 's (e.g., at $t = -3.5$ and 0 Gyr) is:

$$\frac{B'}{B} = \frac{s_i + \Psi}{s_i + \Psi'} \approx \frac{-18.85 + 50.38}{-18.85 + 176} = 0.2, \quad (16)$$

where we used $s_i = s_3 \approx -18.85''/\text{y}$ (largest forcing term for Earth), $\Psi \approx 50.38''/\text{y}$ (at present), and $\Psi' \approx 176''/\text{y}$ (at -3.5 Gyr, see Fig. 5b). Given $\max\{B\} \approx 2.4$ deg over the past 10 Myr, we estimate $\max\{B'\} \approx 0.48$ deg at -3.5 Gyr. Indeed, ϵ 's maximum amplitude in our numerical integration is ~ 0.45 deg around -3.5 Gyr (see Fig. 5c). Notably, while analyzing the results of the present computations, a paper by Ito et al. (1993) was brought to our attention that used a different approach but also found low power in obliquity terms on Gyr-time scale in the past. In summary, a reduced obliquity amplitude in the past is expected from first principles and is quantitatively consistent with our numerical solutions (see Discussion).

We include error estimates (envelopes) for our results based on estimated lunar distance uncertainties (reflecting the cyclostratigraphic data errors, see Fig. 5a). The uncertainties in a_L (minimum/maximum) are propagated through PT integrations with `snvec` using tidal time lags Δt_i 's (see Fig. 1) that produce a_L curves coinciding with the lower/upper envelope bounds (Fig. 5a). This procedure provides propagated errors for Ψ (Fig. 5b) and ϵ , where the latter also depend on the OS (for details on ϵ errors and a comparison to Waltham (2015)'s results, see Appendix F, Fig. F2).

4.4 Example solutions and spectra

Solar system chaos prevents identifying a unique solution on time scales $\gtrsim 10^8$ y. Hence we present results from a few example solutions (and their spectra over selected time intervals) that exhibit typical and/or notable behavior. The solution R02 shows a somewhat typical eccentricity-tilt-precession (ETP) pattern, without σ_{12} -resonance intervals (see Fig. 6). Note the typical rise in ϵ and its amplitude and the drop in ϵ - and $\dot{\beta}$ -frequencies with time. For the spectral analysis (MTM), we selected 5-Myr windows and an ETP composite with relative weights of [1 0.8 0.5] centered around -3 , -2 , -1 , and 0 Gyr (see Fig. 7). The ETP composite was selected so that roughly equal power is represented in each frequency band (E/T/P) in the most recent past (0 Gyr). The MTM power spectrum of R02 illustrates the typical power and frequency evolution for eccentricity and precession, and highlights the common rise in obliquity power over time (Fig. 7, top row). At $t = -1$, -2 , and -3 Gyr, spectral obliquity power based on R02 is reduced to about 50%, 10%, and 5% of its recent value. In contrast to R02, the solution R28 includes σ_{12} -resonance intervals and shows substantially reduced LEC power at, e.g., -2 and -1 Gyr (Fig. 7, bottom row). For details on the unstable LEC and the σ_{12} resonance, see Appendix D and Zeebe & Lantink (2024a).

4.5 Summary of ETP periods

From our ensemble integrations, we construct an overview of the ETP periods over time (Fig. 8). The periods of the relevant long- and short eccentricity cycles (LEC and SEC) are given by combinations of $g_i - g_j$. The dominant obliquity frequencies are given by $\Psi + s_i$, with $i = 1, \dots, 4, 6$. While the s_i vary somewhat over time (see Fig. 2), by far the largest change in obliquity periods over time is due to Ψ (see Fig. 5b). A similar argument holds for the dominant precession frequencies given by $\Psi + g_i$,

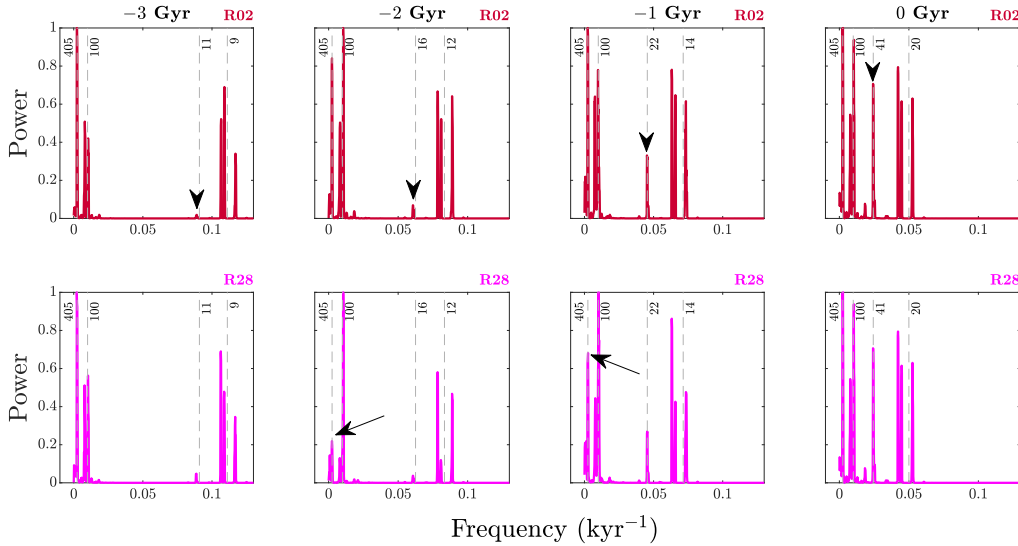


Figure 7. MTM analysis using 5-Myr windows and an ETP composite with relative weights of [1 0.8 0.5] centered around -3 , -2 , -1 , and 0 Gyr. Vertical dashed lines and numbers indicate periods in kyr. Top row: solution R02. Note rise in obliquity power over time (arrows). Bottom row: solution R28. Note substantially reduced LEC power at -2 and -1 Gyr during σ_{12} -resonance intervals due to weaker g_2 in $g_2 - g_5$ (arrows). At the same time, the SEC power is reduced around ~ 125 - 130 kyr ($g_3 - g_2$ and $g_4 - g_2$, see Fig. 8), consistent with a weaker g_2 .

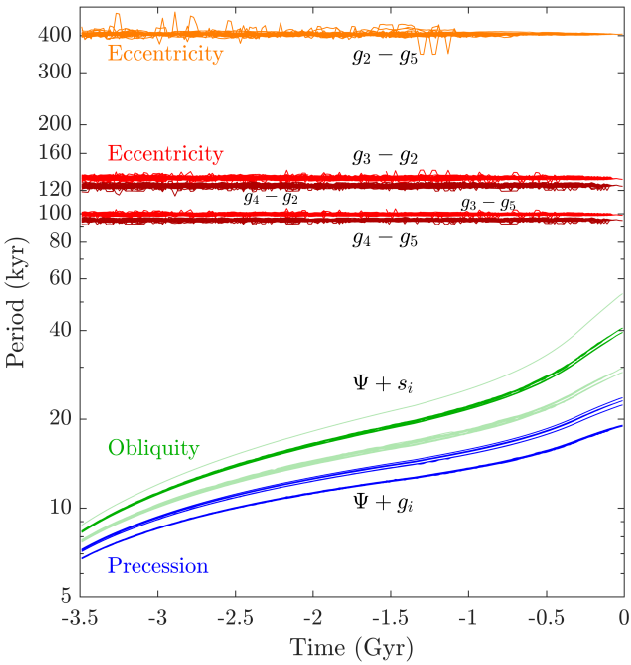


Figure 8. Summary of ETP periods from our 3.5-Gyr solutions. Note the logarithmic ordinate. TP periods are plotted for the g_i 's and s_i 's of all OS ensemble members, while Ψ was taken from the PT solution based on OS R06 (Ψ is nearly identical for all OSs).

with $i = 1, \dots, 5$. The implications of our findings are discussed in Section 5.

5 Discussion

5.1 Precession-Obliquity evolution

Our approach yields a reduced obliquity amplitude in the past (Fig. 5c), which is expected from first principles and is quantitatively consistent with our numerical solutions (see also Ito et al., 1993). We therefore predict weaker climate forcing at obliquity frequencies in deep time and a trend toward reduced obliquity power with age in stratigraphic records. In addition, a smaller overall obliquity (polar angle) reduces seasonality and would contribute to a muted (high-latitude) climate response to obliquity forcing in the distant past.

5.2 Summary of ETP periods

5.2.1 SEC

Compared to the LEC, the SEC is generally considered a poor tuning target in deep time because its exact pattern is unpredictable beyond ~ 50 Myr, as all four SEC components involve either g_3 or g_4 (see Fig. 8), which are affected by solar system chaos on that time scale. In addition, while the LEC consists of a single component, the SEC consists of four components, which can rarely, if ever, be extracted individually from geologic records. However, considering that there were likely intervals of past LEC ($g_2 - g_5$) instability (Zeebe & Lantink, 2024a), could the SEC represent a potential alternative as a primary stratigraphic tuning target?

In our Gyr-simulations, the SEC periods turned out to be relatively stable, despite some variations (Fig. 8). Assume for now that the two main SEC pairs (~ 95 - 100 kyr and ~ 125 - 130 kyr) can be extracted from a stratigraphic record (usually requires high-quality records). For a stable tuning target, SEC components based on combinations including g_2 (~ 125 - 130 kyr) may be less favorable though because of g_2 's involvement in the σ_{12} resonance, which would then leave $g_3 - g_5$ and $g_4 - g_5$ as targets (~ 95 - 100 kyr). As discussed above, g_3 and g_4 do show varia-

tions in frequency and hence period, whereas g_5 is practically stable (see Fig. 2). More importantly, however, g_3 and g_4 show substantial variations in spectral power. For instance, the g_4/g_3 power ratio may vary by a factor of 10 to 100 across a single 3.5-Gyr solution. As a result, the dominant astronomical SEC power switches between frequencies over time, which renders their identification in a record ambiguous. Moreover, if $g_3 - g_2$ or $g_4 - g_2$ is strong during parts of such intervals, and when time series analysis of the geologic sequence yields only a single peak around the SEC periods, ambiguities and uncertainties in period assignment may worsen. For comparison, in our simulations, the combined SEC components span a wide range from $\min\{g_4 - g_5\} \approx 92$ kyr to $\max\{g_3 - g_2\} \approx 141$ kyr. Note that these numbers reflect *individual SEC periods* extracted from astronomical solutions, whereas a dominant SEC peak extracted from cyclostratigraphic sequences may only reflect an *average SEC duration* due to the nonlinear response of the climate-depositional system and/or insufficient sampling, spectral resolution, etc. (see Lantink et al., 2022). In summary, using the SEC as an alternative primary stratigraphic tuning target in deep time would likely be challenging in most cases.

5.2.2 Deep-time obliquity and precession frequencies

It appears that obliquity and precession frequencies may be more difficult to distinguish in deep-time stratigraphic records older than ~ 2.5 Ga or so (see Fig. 8). However, given the trend of weaker climate forcing at obliquity frequencies with age, this might be less of a problem, as precession power would dominate over obliquity power (see Figs. 6 and 7). Importantly though, the precession dominance applies to the orbital forcing, not necessarily the ultimate cyclostratigraphic expression, which is generally modulated/modified by climate-depositional system. Also, because our computations predict the most reduced obliquity forcing beyond about -1 Gyr (Figs. 6 and 7), we expect the most significant implications for cyclostratigraphic and paleoclimate studies involving obliquity for Mesoproterozoic to Archean time intervals.

6 Conclusions

We have presented internally consistent orbital and precession-tilt solutions, including results for the fundamental (secular) solar system frequencies, orbital eccentricity and inclination, lunar distance, luni-solar precession rate, Earth’s obliquity, and climatic precession over the past 3.5 Gyr. Our goal is to make our theoretical framework widely accessible, stimulate computational and observational progress, and assist in the interpretation of deep-time cyclostratigraphic records and the design of external forcing functions in climate models. Our numerical output is available at 400-year resolution at www.ncei.noaa.gov/access/paleo-search/study/39199 and www2.hawaii.edu/~zeebe/Astro.html. Some of our long-term objectives align closely with Milanković, i.e., “... be able to determine the most important basic features of the Earth’s climate computationally.” (Milanković, 1941). However, we advocate that achieving the objective requires a synthesis of both, theoretical and observational efforts.

Open Research | Data and Software Availability Statement

The software associated with this manuscript for the solar system integrations (orbitN, version 1.0.0) has been published on Zenodo (Zeebe, 2023a, 2023b) and GitHub (github.com/rezeebe/orbitN). Data has been deposited at Zeebe (2024).

Acknowledgments. We thank the three reviewers for constructive comments, which improved the manuscript. We also thank Steve Meyers for bringing the paper by Ito et al. (1993) to our attention. This research was supported by Heising-Simons Foundation grants #2021-2800 and #2021-2797 (R.E.Z. and M.L.L.) and U.S. NSF grants OCE20-01022, OCE20-34660 to R.E.Z.

Appendix A Milanković quote

In lieu of a footnote (not permitted) we provide here the original quote cited in Section 1 (Milanković, 1941): “Wenn es tatsächlich gelingen sollte [...] eine mathematische Theorie zu schaffen, mittels der man die Wirkungen der Sonnenstrahlung in Raum und Zeit verfolgen könnte, so wäre man vor allem in der Lage, die wichtigsten Grundzüge des Erdklimas rechnerisch zu ermitteln.”

Appendix B Precession constant

The calculation of precession and obliquity using our snvec code is detailed in Zeebe (2022). A few equations for the precession constant are included here for completeness. The change in the spin axis (unit vector \mathbf{s}) is calculated from (e.g., Goldreich, 1966; Ward, 1974, 1979; Bills, 1990; Quinn et al., 1991; Ito et al., 1995):

$$\dot{\mathbf{s}} = \alpha(\mathbf{n} \cdot \mathbf{n})(\mathbf{s} \times \mathbf{n}), \quad (\text{B1})$$

where α is the precession constant and \mathbf{n} the orbit normal (unit vector normal to the orbit plane). The obliquity (polar) angle, ϵ , is given by:

$$\cos \epsilon = \mathbf{n} \cdot \mathbf{s}. \quad (\text{B2})$$

The precession (azimuthal) angle, ϕ , measures the motion of \mathbf{s} in the orbit plane. The precession constant α is calculated from (Quinn et al., 1991):

$$\alpha = K(\kappa + \beta), \quad (\text{B3})$$

where $\kappa = (1 - e^2)^{-3/2}$ and e is the orbital eccentricity. K and β relate to the torque due to the Sun and Moon, respectively (Quinn et al., 1991):

$$K = \frac{3}{2} \frac{C - A}{C} \frac{1}{\omega a^3} GM \quad (\text{B4})$$

$$\beta = g_L \frac{a^3 m_L}{a_L^3 M}, \quad (\text{B5})$$

where A and C are the planet’s equatorial and polar moments of inertia, $(C - A)/C = E_d$ is the dynamical ellipticity, ω is Earth’s angular speed, a the semi-major axis of its orbit, a_L is the Earth-Moon distance parameter, and GM is the gravitational parameter of the Sun (see Table 1). The index ‘L’ refers to lunar properties, where g_L is a correction factor related to the lunar orbit (Kinoshita, 1975, 1977; Quinn et al., 1991) and m_L/M is the lunar to solar mass ratio. The parameter values used for Earth are given in Table 1. With K and β , the luni-solar precession rate Ψ can be calculated (see Eq. (15)).

Appendix C Numerical integrator and physical setup

Our integrator package `orbitN` (v1.0) (Zeebe, 2023a) uses a 2nd order symplectic integrator and Jacobi coordinates (Wisdom & Holman, 1991; Zeebe, 2015a); the open source code is available at doi.org/10.5281/zenodo.8021040 and github.com/rezeebe/orbitN. Solar system integrations were carried out following our earlier work for which methods and integrator have been extensively tested and compared against other studies (Zeebe, 2015a; Zeebe, 2015b; Zeebe, 2017; Zeebe & Lourens, 2019; Zeebe, 2022; Zeebe, 2023a). For the present study, we also included simulations with an independent integrator package (HNBody) (Rauch & Hamilton, 2002) and found essentially the same dynamical behavior. All simulations include contributions from general relativity, available in `orbitN` as Post-Newtonian effects due to the dominant mass (Saha & Tremaine, 1994). The Earth-Moon system was modeled as a gravitational quadrupole (Quinn et al., 1991; Varadi et al., 2003; Zeebe, 2017; Zeebe, 2023a). Initial conditions for the positions and velocities of the planets and Pluto were generated from the latest JPL ephemeris DE441 (Park et al., 2021) using the SPICE toolkit for Matlab. Coordinates were obtained at JD2451545.0 in the ECLIPJ2000 reference frame and subsequently rotated to account for the solar quadrupole moment (J_2) alignment with the solar rotation axis (Zeebe, 2017). Solar mass loss was included using $\dot{M}/M = -7 \times 10^{-14} \text{ y}^{-1}$ (e.g., Quinn et al., 1991). Quinn et al.'s value falls toward the lower end of more recent solar mass loss estimates (e.g., Minton & Malhotra, 2007; Fienga & Minazzoli, 2024), which is likely of minor importance though. In additional eight test simulations (not shown), we used a very large solar mass loss of $\dot{M}/M = -1.1 \times 10^{-11} \text{ y}^{-1}$ (Spalding et al., 2018) and found again essentially the same dynamics, including σ_{12} -resonance episodes. One consequence of the large mass loss is of course a substantial secular trend in fundamental frequencies (see Spalding et al., 2018).

As solar mass loss also causes a secular drift in total energy, we added test runs with $\dot{M} = \text{const.}$ to check the integrator's numerical accuracy. Total energy and angular momentum errors were small throughout the 3.5-Gyr integrations (relative errors: $\lesssim 6 \times 10^{-10}$ and $\lesssim 7 \times 10^{-12}$, see Zeebe & Lantink (2024a)). The current simulations did not consider asteroids, which is numerically expensive when included as fully gravitationally interacting bodies. Asteroids are quite important for, e.g., high-fidelity solutions on 100-Myr time scale, when probing for sensitivities to dynamical chaos. However, the current goal is to explore the general solution/phase space of the system and provide characteristic features of long-term forcing and fundamental frequencies, which is unlikely to be affected by asteroids due to their small mass. Our default numerical timestep ($|\Delta t| = 4$ days) is close to the previously suggested value of 3.59 days to sufficiently resolve Mercury's perihelion (Wisdom, 2015; Hernandez et al., 2022; Abbot et al., 2023). In additional eight simulations, we tested $|\Delta t| = 2.15625$ days (adequate to $e_{\text{g}} \lesssim 0.4$) and found no differences in the results, including in terms of σ_{12} resonances (see Appendix D and Zeebe & Lantink (2024a)), which occurred in 3/8 solutions.

Appendix D Long eccentricity cycle and σ_{12} resonance

As detailed in Zeebe & Lantink (2024a), we found that the long eccentricity cycle (LEC) can become unstable over long time scales, without major changes in, or destabilization of, planetary orbits. The LEC's disruption is due to a secular resonance between the apsidal and nodal precession frequencies dominated by Mercury's and Venus' orbits and is a major contributor to solar system chaos. Entering/exiting the secular resonance is a common phenomenon on long time scales, occurring in $\sim 40\%$ of our astronomical solutions. During resonance episodes, the LEC is very weak or absent and Earth's orbital eccentricity and climate-forcing spectrum are unrecognizable compared to the recent past. These findings have fundamental implications for paleoclimatology, astrochronology, and cyclostratigraphy because the paradigm that the longest Milanković cycle dominates Earth's climate forcing, is stable, and has a period of ~ 405 kyr requires revision (Zeebe & Lantink, 2024a).

Appendix E Tidal torques

E1 Mignard's torques

As our default option, we use Mignard's tidal torques, including solar-lunar cross terms (Mignard, 1981; Touma & Wisdom, 1994). The equations can be written succinctly using abbreviations following Goldreich (1966):

$$\begin{aligned} x &= (\mathbf{s} \cdot \mathbf{n}) = \cos \epsilon; & y &= (\mathbf{b} \cdot \mathbf{n}) = \cos i_L; \\ z &= (\mathbf{s} \cdot \mathbf{b}) = \cos \epsilon^* & & \\ s_x &= (1 - x^2)^{\frac{1}{2}} = \sin \epsilon; & s_y &= (1 - y^2)^{\frac{1}{2}} = \sin i_L; \\ s_z &= (1 - z^2)^{\frac{1}{2}} = \sin \epsilon^*. & & \end{aligned} \quad (\text{E1})$$

Furthermore, we use (a_E = semimajor axis of Earth's orbit):

$$\begin{aligned} A_1 &= \Delta t \frac{k_2 G m_L^2 R_E^5}{a_L^6}; & A_2 &= \Delta t \frac{k_2 G M^2 R_E^5}{a_E^6}; \\ A_{12} &= \Delta t \frac{k_2 G m_L M R_E^5}{a_L^3 a_E^3} \end{aligned} \quad (\text{E3})$$

and

$$\begin{aligned} u &= \cos(\Omega - \Omega_{\text{g}}) = (y - xz)/(s_x s_z); \\ u_2 &= \cos 2(\Omega - \Omega_{\text{g}}) = 2u^2 - 1, \end{aligned} \quad (\text{E4})$$

where Ω and Ω_{g} are the ascending nodes of the lunar and solar orbits on the equator plane. The torque components in Goldreich's coordinate projection are given by:

$$\mathbf{T} \cdot \mathbf{s} = T_2 s_z + T_3 z + T_2' s_x + T_3' x \quad (\text{E5})$$

$$\mathbf{T} \cdot \mathbf{b} = T_3 - T_1' w/s_x + T_2'(z - xy)/s_x + T_3' y \quad (\text{E6})$$

$$\mathbf{T} \cdot \mathbf{n} = T_1 w/s_z + T_2(x - yz)/s_z + T_3 y + T_3'. \quad (\text{E7})$$

Following Goldreich (1966) and Touma & Wisdom (1994), we assume negligible contributions from T_1 and T_1' terms and drop them. Using $f_2 = (x - yz)/s_z$ and $f_2' = (z - xy)/s_x$, the components T_i and T_i' can be easily identified (see below). The torques below are given for the Moon and

are opposite for the Earth. Then, the average lunar torques due to lunar tides can be written as:

$$T \cdot s = A_1 \left[\frac{3}{2} \omega s_z^2 + 3z(\omega z - n_L) \right] = T_2 s_z + T_3 z \quad (\text{E8})$$

$$T \cdot b = A_1 [3(\omega z - n_L)] = T_3 \quad (\text{E9})$$

$$T \cdot n = A_1 \left[\frac{3}{2} \omega(x - yz) + 3y(\omega z - n_L) \right] = T_2 f_2 + T_3 y. \quad (\text{E10})$$

The average solar torques due to solar tides are:

$$T \cdot s = A_2 \left[\frac{3}{2} \omega s_x^2 + 3x(\omega x - n_E) \right] = T'_2 s_x + T'_3 x \quad (\text{E11})$$

$$T \cdot b = A_2 \left[\frac{3}{2} \omega(z - xy) + 3y(\omega x - n_E) \right] = T'_2 f'_2 + T'_3 y \quad (\text{E12})$$

$$T \cdot n = A_2 [3(\omega x - n_E)] = T'_3. \quad (\text{E13})$$

The average lunar torques due to solar tides (cross terms) are:

$$T \cdot s = A_{12} \omega \left[\frac{3}{8} s_y^2 s_x^2 u_2 - \frac{9}{8} s_y^2 s_x^2 - \frac{3}{4} x y s_x s_y u + \frac{3}{4} s_x^2 \right] = T'_2 s_x + T'_3 x \quad (\text{E14})$$

$$T \cdot b = 0 \quad (\text{E15})$$

$$T \cdot n = A_{12} \omega \left[-\frac{3}{4} y s_x s_y u \right] = T'_3. \quad (\text{E16})$$

Finally, the average solar torques due to lunar tides (cross terms) are:

$$T \cdot s = A_{12} \omega \left[\frac{3}{8} s_y^2 s_x^2 u_2 - \frac{9}{8} s_y^2 s_x^2 - \frac{3}{4} x y s_x s_y u + \frac{3}{4} s_x^2 \right] = T'_2 s_x + T'_3 x \quad (\text{E17})$$

$$T \cdot b = A_{12} \omega \left[\frac{3}{4} y^2 s_x s_y u - \frac{3}{4} x y s_y^2 \right] \quad (\text{E18})$$

$$T \cdot n = 0. \quad (\text{E19})$$

E2 MacDonald's torques

MacDonald's torques are given by (MacDonald, 1964; Goldreich, 1966) ($T_1 = 0$):

$$T_2 = -T_{2L} = - \left[2 m_L A / (\pi a_L^6) \right] q B(q^2) \sin(2\delta) \quad (\text{E20})$$

$$T_3 = -T_{3L} = - \left[2 m_L A / (\pi a_L^6) \right] q' K(q^2) \sin(2\delta) \quad (\text{E21})$$

$$A = (3/2) G m_L R_E^5 k_2, \quad (\text{E22})$$

where T_i and T_{iL} refer to the Earth and the Moon, respectively, and δ is the tidal phase lag. Furthermore,

$$q^2 = \frac{1 - z^2}{1 + \tilde{\alpha}^2 - 2\tilde{\alpha}z}, \quad (\text{E23})$$

where $z = (s \cdot b) = \cos \epsilon^*$, $\tilde{\alpha} = n_L / \omega$, and $q' = (1 - q^2)^{1/2}$, with $\text{sign } q' = \text{sign}(z - \tilde{\alpha})$. The complete elliptic integrals of the 1st and 2nd kind are denoted as $K(q^2)$ and $E(q^2)$, from which $B(q^2)$ is calculated:

$$B(q^2) = \{E(q^2) - q'^2 K(q^2)\} / q^2. \quad (\text{E24})$$

Appendix F Tidal evolution and error envelopes

In this appendix, we provide additional information on tidal evolution models (Fig. F1) and a comparison of our computed orbital parameters to Waltham (2015), including error envelopes (Fig. F2).

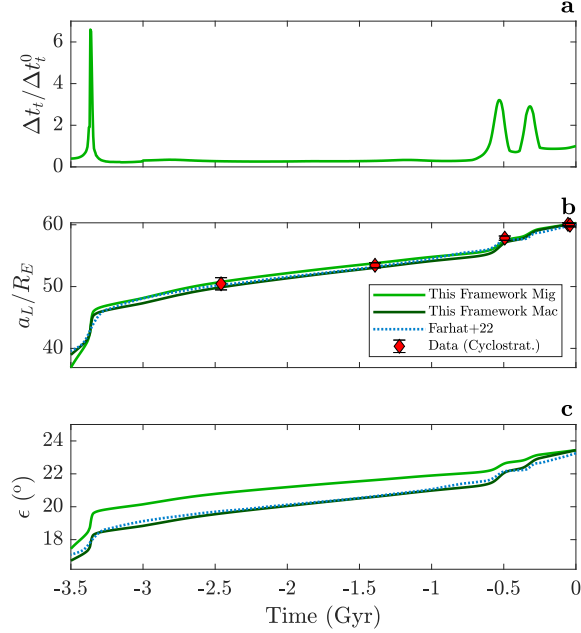


Figure F1. Illustration of evaluating results of ocean tidal evolution models within the current framework. As an example, we select the recent model by Farhat et al. (2022). The point here is to illustrate the procedure, not to reproduce exact results. (a) Tidal time lag (normalized to Δt_t at $t = 0$) used here in Mignard's and MacDonald's torques (Mig and Mac), roughly approximated to resemble Farhat et al. (2022)'s tidal torque history and to match a_L data. (b) Lunar distance (a_L) in units of Earth radii (R_E). Green line: computed using current approach and time lag shown in (a). Dashed blue line: results from Farhat et al. (2022). Red diamonds: Observational estimates based on robust data sets from cyclostratigraphic studies (see Section 3.7). (c) Earth's obliquity ϵ . Larger ϵ values at a given a_L (Mignard's torques) are due to solar-lunar cross-terms (see main text). Otherwise, and for the most part, there are small differences to the current standard approach (see Fig. 5). Importantly, no observational data is presently available to verify or falsify the rapid rise in lunar distance around -3.5 Gyr, see (b). For Earth's obliquity (c), the tidal torque physics are more important here than the details of the tidal history, as long as a_L matches observational data (fitted here using Δt_t).

References

- Abbot, D. S., Hernandez, D. M., Hadden, S., Webber, R. J., Afentakis, G. P., & Weare, J. (2023). Simple Physics and Integrators Accurately Reproduce Mercury Instability Statistics. *Astrophys. J.*, 944(2), 190. doi: 10.3847/1538-4357/acb6ff
- Atobe, K., & Ida, S. (2007). Obliquity evolution of extrasolar terrestrial planets. *Icarus*, 188(1), 1-17. doi: 10.1016/j.icarus.2006.11.022
- Baenas, T., Escapa, A., & Ferrándiz, J. M. (2019). Precession of the non-rigid Earth: Effect of the mass redistribution. *Astron. Astrophys.*, 626, A58. doi: 10.1051/0004-6361/201935472
- Berger, A., Loutre, M. F., & Dehant, V. (1989). Influence of the changing lunar orbit on the astronomical frequencies of pre-Quaternary insolation patterns. *Paleoceanogr.*, 4(5), 555-564. doi: 10.1029/PA004i005p0555

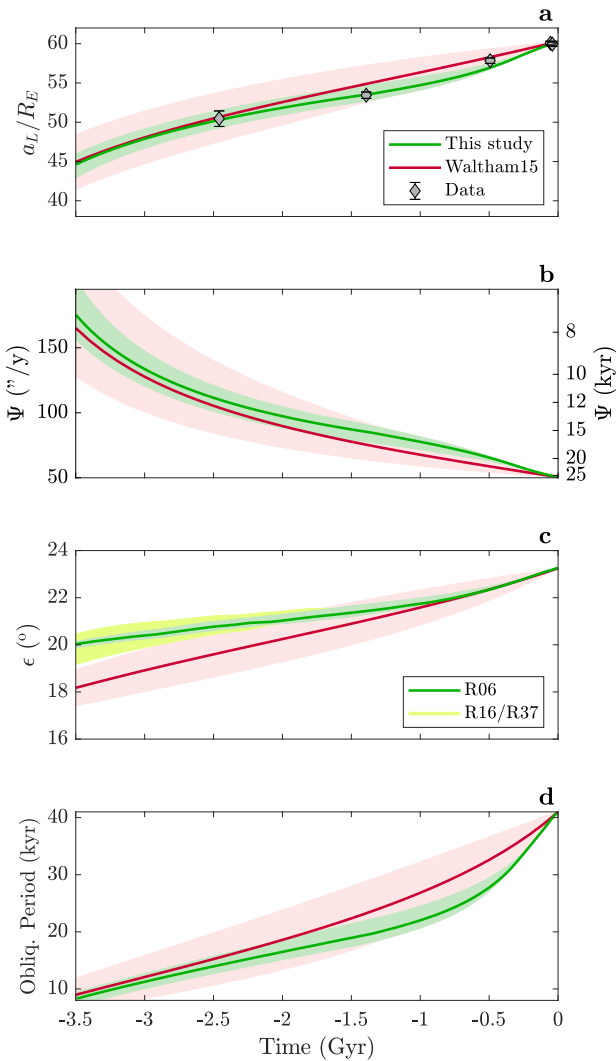


Figure F2. Comparison of the present results (based on OS R06) to those of Waltham (2015), see <http://nm2.rhul.ac.uk/Milankovitch1.html>. Waltham (2015) used a simplified model which neglects solar and solar-lunar cross tides. Light red areas: Error envelope given by Waltham (2015). Light green areas: Error envelope of this study based on estimated lunar distance uncertainties (reflecting the cyclostratigraphic data errors, see panel (a)). (a) Lunar distance (a_L) in units of Earth radii (R_E). Gray diamonds: Observational estimates based on robust data sets from cyclostratigraphic studies (see Section 3.7). (b) Luni-solar precession rate (Ψ) in arcsec y^{-1} (left axis) and period in kyr (right axis). (c) Earth's obliquity ϵ . To facilitate the comparison, the ϵ results of this study (which include the full ϵ amplitude, i.e., variations around the mean) were binned and smoothed. Green-yellow area: Extended error envelope including OSs R16 and R37 (smallest and largest binned ϵ values of ensemble at $t = -3.5$ Gyr). Note that different OSs have little effect on a_L and Ψ . Larger ϵ values at a given time in the past (compared to, and significantly different from, Waltham, 2015) are calculated here using Mignard's torques and are hence due to solar-lunar cross-terms (see Touma & Wisdom, 1994). (d) Obliquity period.

Bills, B. G. (1990). The rigid body obliquity history of Mars. *J. Geophys. Res.*, 95, 14137–14153. doi: 10.1029/JB095iB09p14137

Capitaine, N., Wallace, P. T., & Chapront, J. (2003). Expressions for IAU 2000 precession quantities. *Astron. Astrophys.*, 412, 567–586. doi: 10.1051/0004-6361:20031539

Cheng, W. H., Lee, M. H., & Peale, S. J. (2014). Complete tidal evolution of Pluto-Charon. *Icarus*, 233, 242–258. doi: 10.1016/j.icarus.2014.01.046

Daher, H., Arbic, B. K., Williams, J. G., Ansong, J. K., Boggs, D. H., Müller, M., ... Huber, M. (2021). Long-Term Earth-Moon Evolution With High-Level Orbit and Ocean Tide Models. *J. Geophys. Res. (Planets)*, 126(12), e06875. doi: 10.1029/2021JE006875

De Vleeschouwer, D., Penman, D. E., D'haenens, S., Wu, F., Westendorp, T., Vahlenkamp, M., ... Hull, P. M. (2023). North Atlantic Drift Sediments Constrain Eocene Tidal Dissipation and the Evolution of the Earth-Moon System. *Paleoceanogr. Paleoclim.*, 38(2), 4555. doi: 10.1029/2022PA004555

De Vleeschouwer, D., Percival, L. M., Wichern, N. M., & Batenburg, S. J. (2024). Pre-Cenozoic cyclostratigraphy and palaeoclimate responses to astronomical forcing. *Nature Rev. Earth Env.*, 5, 59–74.

Downey, B. G., Nimmo, F., & Matsuyama, I. (2023). The thermal-orbital evolution of the Earth-Moon system with a subsurface magma ocean and fossil figure. *Icarus*, 389, 115257. doi: 10.1016/j.icarus.2022.115257

Efroimsky, M., & Makarov, V. V. (2013). Tidal Friction and Tidal Lagging. Applicability Limitations of a Popular Formula for the Tidal Torque. *Astrophys. J.*, 764(1), 26. doi: 10.1088/0004-637X/764/1/26

Farhat, M., Auclair-Desrotour, P., Boué, G., & Laskar, J. (2022). The resonant tidal evolution of the Earth-Moon distance. *Astron. Astrophys.*, 665, L1. doi: 10.1051/0004-6361/202243445

Fienga, A., & Minazzoli, O. (2024). Testing theories of gravity with planetary ephemerides. *Living Reviews in Relativity*, 27(1), 1–99. doi: 10.1007/s41114-023-00047-0

Fränz, M., & Harper, D. (2002). Heliospheric coordinate systems. *Planet. Space Sci.*, 50, 217–233. doi: 10.1016/S0032-0633(01)00119-2

Goldreich, P. (1966). History of the lunar orbit. *Rev. Geophys. Space Phys.*, 4, 411–439. doi: 10.1029/RG004i004p00411

Hansen, K. S. (1982). Secular effects of oceanic tidal dissipation of the moon's orbit and the earth's rotation. *Rev. Geophys. Space Phys.*, 20, 457–480. doi: 10.1029/RG020i003p00457

Hernandez, D. M., Zeebe, R. E., & Hadden, S. (2022). Step-size errors in the N-body problem: discerning Mercury's true possible long-term orbits. *MNRAS*, 510(3), 4302–4307. doi: 10.1093/mnras/stab3664

Hinnov, L. A. (2018). Cyclostratigraphy and Astrochronology in 2018. In M. Montenari (Ed.), *Stratigraphy & timescales* (Vol. 3, p. 1–80). Elsevier.

Hoang, N. H., Mogavero, F., & Laskar, J. (2021). Chaotic diffusion of the fundamental frequencies in the Solar System. *Astron. Astrophys.*, 654, A156. doi: 10.1051/0004-6361/202140989

Ito, T., Kumazawa, M., Hamano, Y., Matsui, T., & Masuda, K. (1993). Long Term Evolution of the Solar Insolation Variation over 4Ga. *Proc. Japan Acad., Series B*, 69(9), 233–237. doi: 10.2183/pjab.69.233

Ito, T., Masuda, K., Hamano, Y., & Matsui, T. (1995). Climate friction: A possible cause for secular drift of Earth's obliquity. *J. Geophys. Res.*, 100(B8), 15147–15162. doi: 10.1029/95JB01061

Kagan, B. A., & Maslova, N. B. (1994). A Stochastic Model of the Earth-Moon Tidal Evolution Accounting for Cyclic Variations of Resonant Properties of the Ocean: An Asymptotic Solution. *Earth, Moon and Planets*, 66(2), 173–188. doi: 10.1007/BF00644130

Kinoshita, H. (1975). Formulas for Precession. *SAO Special Report*, 364.

Kinoshita, H. (1977). Theory of the Rotation of the Rigid Earth. *Celestial Mechanics*, 15(3), 277–326. doi: 10.1007/BF01228425

Lambeck, K. (1980). *The Earth's variable rotation: Geophysical causes and consequences*. Cambridge University Press, p. 449.

Lantink, M. L., Davies, J. H. F. L., Hennekam, R., Martin, D. M., Mason, P. R. D., Reichart, G., & Hilgen, F. J. (2024). Towards an astrochronological framework for the lower Paleoproterozoic Kuruman and Brockman Iron Formations. *South African J. Geol., Special Issue*. doi: doi.org/10.31223/X51H4D

Lantink, M. L., Davies, J. H. F. L., Mason, P. R. D., Schaltegger, U., & Hilgen, F. J. (2019). Climate control on banded iron formations linked to orbital eccentricity. *Nature Geosci.*, 12(5), 369–374. doi: 10.1038/s41561-019-0332-8

Lantink, M. L., Davies, J. H. F. L., Ovtcharova, M., & Hilgen, F. J. (2022). Milankovitch cycles in banded iron formations constrain the Earth-Moon system 2.46 billion years ago. *Proc. Nat. Acad. Sci.*, 119(40), e2117146119. doi: 10.1073/pnas.2117146119

Laskar, J., Farhat, M., Lantink, M. L., Auclair-Desrotour, P., Boué, G., & Sinnesael, M. (2024). Did atmospheric thermal tides cause a daylength locking in the Precambrian? A review on recent results. *Sedimentologica*, 2, 1–15. doi: 10.57035/journals/sdk.2024.e21.1271

Laskar, J., & Gastineau, M. (2009). Existence of collisional trajectories of Mercury, Mars and Venus with the Earth. *Nature*, 459, 817–819. doi: 10.1038/nature08066

Laskar, J., Robutel, P., Joutel, F., Gastineau, M., Correia, A. C. M., & Levrard, B. (2004). A long-term numerical solution for

- the insolation quantities of the Earth. *Astron. Astrophys.*, 428, 261–285. DOI: 10.1051/0004-6361/20041335.
- Lithwick, Y., & Wu, Y. (2011). Theory of secular chaos and Mercury's orbit. *Astrophys. J.*, 739, 17 pp. doi: 10.1088/0004-637X/739/1/31
- Ma, C., Meyers, S. R., & Sageman, B. B. (2017). Theory of chaotic orbital variations confirmed by Cretaceous geological evidence. *Nature*, 542, 468–470. doi: 10.1038/nature21402
- MacDonald, G. J. F. (1964). Tidal Friction. *Rev. Geophys. Space Phys.*, 2, 467–541. doi: 10.1029/RG002i003p00467
- Meyers, S. R., & Malinverno, A. (2018). Proterozoic Milankovitch cycles and the history of the solar system. *Proceedings of the National Academy of Science*, 115(25), 6363–6368. doi: 10.1073/pnas.1717689115
- Mignard, F. (1981). The Lunar Orbit Revisited, III. *Moon and Planets*, 24(2), 189–207. doi: 10.1007/BF00910608
- Milanković, M. (1941). (in German) *Kanon der Erdbestrahlung und seine Anwendung auf das Eiszeitproblem*. Belgrad: Königl. Serb. Akad., pp. 633.
- Minton, D. A., & Malhotra, R. (2007). Assessing the Massive Young Sun Hypothesis to Solve the Warm Young Earth Puzzle. *Astrophys. J.*, 660(2), 1700–1706. doi: 10.1086/514331
- Mogavero, F., & Laskar, J. (2022). The origin of chaos in the Solar System through computer algebra. *Astron. Astrophys.*, 662, L3. doi: 10.1051/0004-6361/202243327
- Montenari, M. (2018). (Editor) *Stratigraphy & Timescales: Cyclostratigraphy and Astrochronology in 2018* (Vol. 3). Elsevier.
- Motoyama, M., Tsunakawa, H., & Takahashi, F. (2020). Tidal resonance of eigenmode oscillation in the early Earth's ocean and its acceleration effect on the Moon's orbital evolution. *Icarus*, 335, 113382. doi: 10.1016/j.icarus.2019.07.016
- Murray, C. D., & Dermott, S. F. (1999). *Solar system dynamics*. Cambridge, UK: Cambridge University Press, pp. 592.
- Olsen, P. E., Laskar, J., Kent, D. V., Kinney, S. T., Reynolds, D. J., Sha, J., & Whiteside, J. H. (2019). Mapping solar system chaos with the geological orrery. *Proc. Nat. Acad. Sci.*, 116(22), 10664–10673. doi: 10.1073/pnas.1813301116
- Park, R. S., Folkner, W. M., Williams, J. G., & Boggs, D. H. (2021). The JPL Planetary and Lunar Ephemerides DE440 and DE441. *Astron. J.*, 161(3), 105. doi: 10.3847/1538-3881/abd414
- Quinn, T. R., Tremaine, S., & Duncan, M. (1991). A three million year integration of the earth's orbit. *Astron. J.*, 101, 2287–2305. doi: 10.1086/115850
- Rauch, K. P., & Hamilton, D. P. (2002). The HNBODY package for symplectic integration of nearly-Keplerian systems. In *As/division of dynamical astronomy meeting #33* (Vol. 34, p. 938).
- Saha, P., & Tremaine, S. (1994). Long-Term Planetary Integration With Individual Time Steps. *Astron. J.*, 108, 1962. doi: 10.1086/117210
- Sinnesael, M., De Vleeschouwer, D., Zeeden, C., Batenburg, S. J., Da Silva, A.-C., de Winter, N. J., ... Claeys, P. (2019). The Cyclostratigraphy Intercomparison Project (CIP): consistency, merits and pitfalls. *Earth Sci. Rev.*, 199, 102965. doi: 10.1016/j.earscirev.2019.102965
- Sørensen, A. L., Nielsen, A. T., Thibault, N., Zhao, Z., Schovsbo, N. H., & Dahl, T. W. (2020). Astronomically forced climate change in the late Cambrian. *Earth Planet. Sci. Lett.*, 548, 116475. doi: 10.1016/j.epsl.2020.116475
- Spalding, C., Fischer, W. W., & Laughlin, G. (2018). An Orbital Window into the Ancient Sun's Mass. *Astrophys. J. Lett.*, 869, L19. doi: 10.3847/2041-8213/aaf219
- Touma, J., & Wisdom, J. (1994, November). Evolution of the Earth-Moon System. *Astron. J.*, 108, 1943. doi: 10.1086/117209
- Tyler, R. H. (2021). On the Tidal History and Future of the Earth-Moon Orbital System. *Planet. Sci. J.*, 2(2), 70. doi: 10.3847/PSJ/abe53f
- Varadi, F., Runnegar, B., & Ghil, M. (2003). Successive refinements in long-term integrations of planetary orbits. *Astrophys. J.*, 592, 620–630. doi: 10.1086/375560
- Waltham, D. (2015). Milankovitch Period Uncertainties and Their Impact On Cyclostratigraphy. *J. Sediment. Res.*, 85(8), 990–998. doi: 10.2110/jsr.2015.66
- Ward, W. R. (1974). Climatic variations on Mars: 1. Astronomical theory of insolation. *J. Geophys. Res.*, 79(24), 3375. doi: 10.1029/JC079i024p03375
- Ward, W. R. (1979). Present obliquity oscillations of Mars: fourth-order accuracy in orbital e and I . *J. Geophys. Res.*, 84, 237–241. doi: 10.1029/JB084iB01p00237
- Ward, W. R. (1982). Comments on the long-term stability of the Earth's obliquity. *Icarus*, 50(2–3), 444–448. doi: 10.1016/0019-1035(82)90134-8
- Webb, D. J. (1982). Tides and the evolution of the earth-moon system. *Geophys. J. R. Astr. Soc.*, 70, 261–271. doi: 10.1111/j.1365-246X.1982.tb06404.x
- Williams, J. G. (1994). Contribution to the Earth's Obliquity Rate, Precession, and Nutation. *Astron. J.*, 108, 711. doi: 10.1086/117108
- Wisdom, J. (2015). Resolving the Pericenter. *Astron. J.*, 150(4), 127. doi: 10.1088/0004-6256/150/4/127
- Wisdom, J., & Holman, M. (1991). Symplectic maps for the n-body problem. *Astron. J.*, 102, 1528–1538. doi: 10.1086/115978
- Zeebe, R. E. (2015a). Dynamic stability of the Solar System: Statistically inconclusive results from ensemble integrations. *Astrophys. J.*, 798, 8. doi: 10.1088/0004-637X/798/1/8
- Zeebe, R. E. (2015b). Highly stable evolution of Earth's future orbit despite chaotic behavior of the Solar System. *Astrophys. J.*, 811, 9. doi: 10.1088/0004-637X/811/1/9
- Zeebe, R. E. (2017). Numerical Solutions for the Orbital Motion of the Solar System over the Past 100 Myr: Limits and New Results. *Astron. J.*, 154, 193. doi: 10.3847/1538-3881/aa8cce
- Zeebe, R. E. (2022). Reduced variations in Earth's and Mars' orbital inclination and Earth's obliquity from 58 to 48 Myr ago due to solar system chaos. *Astron. J.*, 164, 107. doi: 10.3847/1538-3881/ac80f8
- Zeebe, R. E. (2023a). OrbitN: A Symplectic Integrator for Planetary Systems Dominated by a Central Mass – Insight into Long-term Solar System Chaos. *Astron. J.*, 166. doi: 10.3847/1538-3881/acd63b
- Zeebe, R. E. (2023b). orbitN: A Symplectic integrator for near-Keplerian planetary systems. In *The Astronomical Journal* (1.0.0, Vol. 166, Number 1, p. 13pp). [Software]. Zenodo. doi: https://doi.org/10.5281/zenodo.8021040
- Zeebe, R. E. (2024). NOAA/WDS Paleoclimatology - Astronomical Solutions 3.49–0 Ga for Earth's Orbital Eccentricity and Inclination. [Dataset]. NOAA National Centers for Environmental Information. doi: https://doi.org/10.25921/tw1n-k204
- Zeebe, R. E., & Lantink, M. L. (2024a). A secular solar system resonance that disrupts the dominant cycle in Earth's orbital eccentricity ($g_2 - g_5$): Implications for astrochronology. *Astron. J.*, 167, 204. doi: doi.org/10.3847/1538-3881/ad32cf
- Zeebe, R. E., & Lourens, L. J. (2019). Solar system chaos and the Paleocene-Eocene boundary age constrained by geology and astronomy. *Science*, 365, 926–929.
- Zeebe, R. E., & Lourens, L. J. (2022a). A deep-time dating tool for paleo-applications utilizing obliquity and precession cycles: The role of dynamical ellipticity and tidal dissipation. *Paleoceanogr. Paleoclim.*, 37, 2021PA004349. doi: 10.1029/2021PA004349
- Zeebe, R. E., & Lourens, L. J. (2022b). Geologically constrained astronomical solutions for the Cenozoic era. *Earth Planet. Sci. Lett.*, 592, 117595. doi: 10.1016/j.epsl.2022.117595
- Zeebe, R. E., Westerhold, T., Littler, K., & Zachos, J. C. (2017). Orbital forcing of the Paleocene and Eocene carbon cycle. *Paleoceanogr.*, 32, 1. doi: 10.1002/2016PA003054
- Zhang, S., Wang, X., Hammarlund, E. U., Wang, H., Mafalda Costa, M., Bjerrum, C. J., ... Canfield, D. E. (2015). Orbital forcing of climate 1.4 billion years ago. *Proc. Nat. Acad. Sci.*, 112(12), E1406–E1413. doi: 10.1073/pnas.1502239112